ARTICLE

Thermal stability of Mg₂Si₀.₃Sn₀.₇ under different heat treatment conditions

Kang Yin[a], Qiang Zhang[a], Yun Zheng[a], Xianli Su[a*], Xinfeng Tang[a*], and Ctirad Uher[b]

Sb-doped $Mg_2Si_{0.3}Sn_{0.7}$ solid solutions were prepared by a two-step solid state reaction method followed by electron-discharge plasma activated sintering (Ed-PAS). Thermal stability was tested by changing heat treatment conditions, i.e., the annealing temperature, the annealing time, the annealing atmosphere and preventive coatings. Mg loss is severe when the solid solutions are annealed in vacuum, due to the high saturated vapor pressure of Mg. As a consequence of the Mg loss, β Sn-Sb alloy formed. However, the solid solutions are oxidized when annealed in air. And this is effectively prevented when the samples are coated with boron nitride (BN) spray. The results showed that $Mg_2Si_{1-x}Sn_x$ can be exposed for long periods of time to temperature up to about 823 K, provided it is protected with specific coatings. However, the structure becomes unstable when the temperature exceeds much beyond 823 K, mainly due to the peritectic reaction. The composition, microstructure and thermoelectric (TE) properties of the annealed samples were carefully explored and critically assessed.

Introduction

Thermoelectric (TE) conversion technology, which is based on the Seebeck effect, shows great potential for recovering waste industrial heat and converting it into electricity, with the advantages of exceptionally high reliability, absence of moving parts, silent operation, and environmental friendliness.[1, 2] The energy conversion efficiency of TE devices depends on the dimensionless figure of merit of TE elements defined as $ZT = S^2\sigma T/\kappa$, where S is the Seebeck coefficient, σ is the electrical conductivity, T is the absolute temperature, and κ is the thermal conductivity.[3-5] The higher the dimensionless figure of merit, the higher the conversion efficiency.[6, 7]

$Mg_2Si_{1-x}Sn_x$ solid solutions consist of abundant, inexpensive, low density, and environmentally friendly elements and attract considerable attention for application as power generators in the intermediate temperature range (300–800 K).[8-12] The primary purpose of forming solid solutions from Mg_2Si and Mg_2Sn is to enhance alloy scattering and thus lower the thermal conductivity.[13-15] It has also been shown that doping with Sb is effective in adjusting the carrier concentration.[16-20] Zaitsev et al[15, 21, 22] and T. J. Zhu et al[23, 24] found that the thermoelectric properties are strongly dependent on the ratio between the contents of Si and Sn, i.e., on the parameter x in $Mg_2Si_{1-x}Sn_x$. Moreover, structural studies indicate that Mg_2Si and Mg_2Sn are not fully miscible and the region of immiscibility typically oc-

curs for values of x between $0.4<x<0.6$.[25, 26] Recently, Liu et al.[27, 28] found that the two conduction bands (a heavy conduction band and a lighter one) converge in energy for compositions with x near 0.65-0.70. The band convergence increases the number of carrier pockets participating in the charge transport, enhances in turn the density of states effective mass and thus increases the Seebeck coefficient. Indeed, solid solutions with $x = 0.7$ reached ZT values of about 1.3 at 750–800 K.[16, 29]

For practical TE application, apart from high ZT, an excellent thermal stability at the intended operational temperature range is of vital importance.[30-32] Recently, first steps in this direction were taken by Bourgeois et al.[33] and Skomedal et al.[34] who studied the thermal stability of $Mg_2Si_{1-x}Sn_x$ ($x = 0.25, 0.6$) between 300–673 K. The studies indicated that the solid solutions start to decompose and oxidize into MgO, Si, and Sn above about 630 K. Furthermore, the decomposition rate of powdered solid solutions was much faster than that of the bulk structures. Coating was employed as an effective remedy to decomposition and oxidation of $Mg_2Si_{1-x}Sn_x$ solid solutions, provided it adhered tightly to the structure and did not react with it.

As already noted, the highest ZT value of doped $Mg_2Si_{1-x}Sn_x$ solid solutions occurs between 750–800 K, yet the thermal stability of the structure at such high temperature has rarely been investigated. We have thus decided to study the thermal stability of Sb-doped $Mg_2Si_{0.3}Sn_{0.7}$ (the composition benefiting from the band convergence as well as being in the miscible range of concentrations) by annealing the structure at two different temperatures (773 K and 823 K), altering the time of annealing (either 360 h or 720 h), changing the atmosphere (vacuum or air), and exploring the effectiveness of coating (no on the composition, microstructure, and TE properties of Sb-

[a.] *State Key Laboratory of Advanced Technology for Materials Synthesis and Processing, Wuhan University of Technology, Wuhan 430070, P. R. China. Emai: suxianli@whut.edu.cn, tangxf@whut.edu.cn*
[b.] *Department of Physics, University of Michigan, Ann Arbor, MI 48109, USA*
Electronic Supplementary Information (ESI) available: [details of any supplementary information available should be included here]. See DOI: 10.1039/x0xx00000x

Journal Name

ARTICLE

Table 1 Annealing conditions applied to samples of the same batch

Sample	1	2	3	4	5	6	7	8
$T_{annealing}$ (K)	-	773	773	773	773	773	773	823
Atmosphere	-	Air	Air	Vacuum	Vacuum	Air	Air	Air
Coatings	-	No	No	No	No	BN	BN	BN
$t_{annealing}$ (h)	-	360	720	360	720	360	720	360

doped $Mg_2Si_{0.3}Sn_{0.7}$ was then characterized in detail.

Experimental

Commercial high purity powders of Mg (99%), Mg_2Si (99.9%), Sn (99.9%), and Sb (99.999%) were employed as the starting materials, and $Mg_{2.16}(Si_{0.3}Sn_{0.7})_{0.98}Sb_{0.02}$ compounds were prepared by a two-step solid state reaction method as described previously.[35, 36] The first synthesis reaction was at 873 K for 24 h, and the second reaction step was carried out at 973 K for 24 h. Final consolidation into an ingot was done by electron-discharge plasma activated sintering (Elenix, Ed-PAS III, Japan). An intentional 8% excess of Mg was used to compensate for the anticipated loss of Mg during the synthesis.[35, 37] The resulting pellets were cut into appropriate sizes for electrical and thermal transport measurements with a diamond disk (Iso-Met 4000 linear precision saw, Buehler, USA).

All samples were prepared from the same batch to make sure that the only variable was a particular heat treatment condition. After cutting into appropriate sizes for transport studies, the samples were subjected to heat treatments described in Table 1. BN coating was applied by spraying about 0.5 mm thick layer of BN spray (Kakentech, Japan). The samples were placed in graphite crucibles which, in turn, were inserted in quartz ampoules for annealing. For samples to be annealed in vacuum, the quartz ampoules were evacuated and sealed; while for those to be annealed in air, the quartz ampoules were left open.

The phase purity and the crystal structure of annealed samples were characterized using a PANalytical X'Pert Empyrean type X-ray diffractometer with Cu K_α radiation. The microstructure of the fractured surface and the composition of secondary phases were characterized by field-emission scanning electron microscopy (FESEM) using a Hitachi SU8020 apparatus equipped with Energy-Dispersive X-ray spectrometer (EDX). The actual chemical composition of the polished samples was analyzed by electron probe microanalysis (EPMA) with the aid of JEOL JXA-8230 system. High resolution transmission electron microscopy (HRTEM) was carried out using a JEOL JEM-2100F equipment together with EDX.

The electrical conductivity and the Seebeck coefficient in the range of 300–800 K were measured simultaneously by the standard four-probe method using an Ulvac-Rico ZEM-3 system under helium atmosphere. The Hall coefficient at 300 K was measured by the van der Pauw method (PPMS-9T, Quantum Design). The carrier concentration and the carrier mobility were calculated from $n = 1/eR_H$ and $\mu_H = \sigma R_H$, respectively. Finally, the thermal conductivity was determined by the equation $\kappa = \lambda C_p \rho$, where λ is the thermal diffusivity obtained by the laser flash method (Netzsch LFA 457), C_p is the specific heat obtained by a differential scanning calorimeter (TA DSC Q20) in argon, and ρ is the density measured by the Archimedes method in alcohol. Thermodynamic characteristics of $Mg_2Si_{1-x}Sn_x$ in the range of 400–853 K were investigated using a TGA/DSC simultaneous thermal analyzer (Netzsch STA449c/3/G) with the heating rate of 10 K/min.

Results and discussion

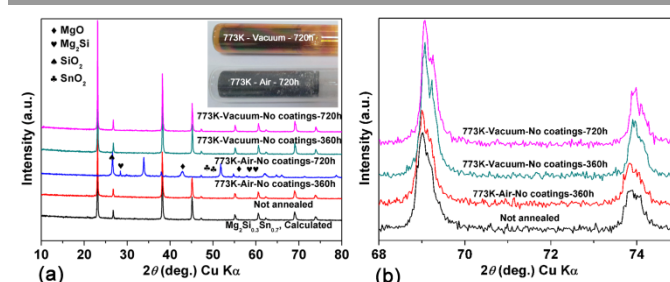### The influence of atmosphere on the composition and microstructure of samples

Fig. 1 (a) XRD patterns of samples annealed at 773 K in vacuum or in air, the inset shows the physical appearance of the quartz ampoules after heat treatment, (b) Enlarged XRD patterns within the angular range of 68-75°.

Since annealing in air or in vacuum are two typical conditions used in industrial processes, we have employed them to study the influence of atmosphere on the composition and microstructure of $Mg_2Si_{1-x}Sn_x$ solid solutions. As shown in the inset of Fig. 1(a), the quartz ampoules acquired different colors depending on the annealing atmosphere,. The brownish coloring of the quartz ampoule after vacuum annealing is believed to originate

Journal Name

ARTICLE

Table 2 Actual compositions of samples annealed in vacuum as determined by EPMA.

Annealing conditions	Not annealed	773 K-Vacuum-No coatings-360 h	773 K-Vacuum-No coatings-720 h
Actual composition	$Mg_{2.13}Si_{0.27}Sn_{0.71}Sb_{0.018}$	$Mg_{2.01}Si_{0.28}Sn_{0.70}Sb_{0.016}$	$Mg_{1.96}Si_{0.28}Sn_{0.70}Sb_{0.016}$

from the reaction $4Mg + SiO_2 \rightarrow Mg_2Si + 2MgO$, as Mg is highly volatile and reactive (details shown in Fig. SI1(a)).

XRD patterns of the annealed $Mg_{2.16}(Si_{0.3}Sn_{0.7})_{0.98}Sb_{0.02}$ samples can be refined in the antifluorite structure with Fm-3m space group,[38] as shown in Fig. 1(a). The reference pattern of $Mg_2Si_{0.3}Sn_{0.7}$ was calculated according to JCPDS#01-089-4254. Though it was still $Mg_2Si_{1-x}Sn_x$ solid solution after annealing in air for 360 h, when time extended to 720 h, the sample oxidized and decomposed into a pile of powder, consisting of MgO, Mg_2Si, SiO_2, and SnO_2, which confirmed the previous findings.[33, 34] Upon annealing in vacuum for either 360 h or 720 h, the XRD peaks shifted to higher angles as evidenced from Fig. 1(b). The decreasing lattice parameter of the vacuum annealed samples (shown in Fig. SI1(b)) arises due to a significant loss of Mg and Sn at elevated temperatures. As the temperature increases, more and more Mg evaporates[45] and the Mg vapor reacts with quartz. To verify the influence of atmosphere on Mg evaporation, we carefully checked the composition of samples after annealing at 773 K in vacuum by EPMA (we randomly selected 10 points in the field of view and then averaged the results, as shown in Table 2). The results showed that the Mg content of the samples decreased by a significant amount after annealing in vacuum and progressively less and less Mg remained in the sample as the annealing timeincreased.

Moreover, the loss of Mg induced the decomposition of $Mg_2Si_{1-x}Sn_x$ matrix into a solid solution with a lower content of Sn and islands rich in Sn and Sb (shown in Table 3). Such islands are clearly visible in Figs 2(b)-(d) as raised grains with the size of 1-2 μm. Since the EDX is semi-quantitative analysis. It is hard to claim the raised grains are pure Sn-Sb alloys. However, DSC traces in Fig. 3(a) show that all vacuum annealed samples display a notable endothermic peak near 700 K. According to the phase diagram,[39, 40] this endothermic peak represents the melting of Sn-Sb alloy. Thus we can speculate that the islands are rich in β Sn-Sb alloy. The presence of the β Sn-Sb alloy not only altered the composition but also weakened the mechanical properties of the material due to differential thermal expansion between the β Sn-Sb alloys and the matrix ($CTE_{Mg2Si1-xSnx}$: 1.7×10^{-5} K^{-1} at room temperature).[41] This is evidenced by the micro-cracks on the rasied grains shown in Fig.2(c). All in all, operating under vacuum is not appropriate for $Mg_2Si_{1-x}Sn_x$ solid solutions as the loss of Mg is serious and triggers structural and compositional changes in the material.
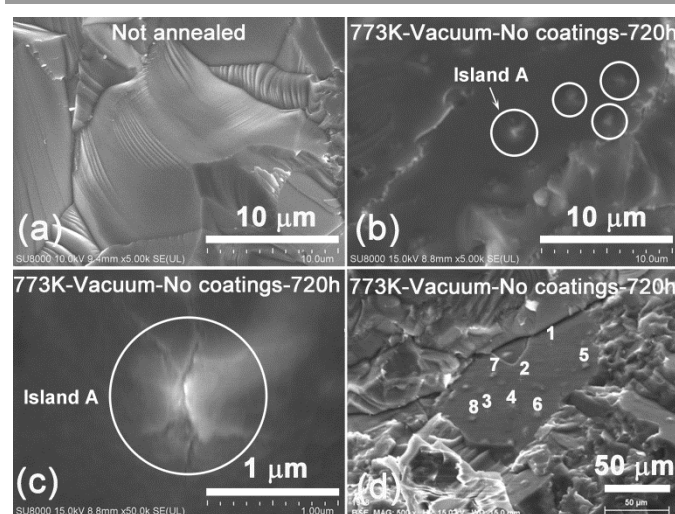
Fig. 2 Microstructure of a sample (a) without annealing, (b)-(d) annealed in vacuum. Cirlces indicate the presence of "islands" like grains after annealing in vacuum, (c) is the enlarged image of island A in (b).

Table 3 EDX results corresponding to points marked in Fig. 2(d)

| Spectrum	Notes	Mg (at.%)	Si (at.%)	Sn (at.%)	Sb (at.%)	composition
1	Matrix	67.27	9.75	22.42	0.55	$Mg_{2.07}Si_{0.30}Sn_{0.69}Sb_{0.017}$
2		67.93	9.66	21.89	0.52	$Mg_{2.11}Si_{0.30}Sn_{0.68}Sb_{0.016}$
3		67.48	9.69	22.28	0.55	$Mg_{2.09}Si_{0.30}Sn_{0.69}Sb_{0.017}$
4		66.97	8.91	23.42	0.69	$Mg_{2.03}Si_{0.27}Sn_{0.71}Sb_{0.021}$
5	The raised grains	65.73	8.56	24.31	1.40	$Mg_{1.92}Si_{0.25}Sn_{0.71}Sb_{0.041}$
6		65.16	8.01	25.78	1.05	$Mg_{1.87}Si_{0.23}Sn_{0.74}Sb_{0.030}$
7		65.73	8.22	24.99	1.06	$Mg_{1.92}Si_{0.24}Sn_{0.73}Sb_{0.031}$
8		65.99	9.48	23.35	1.18	$Mg_{1.95}Si_{0.28}Sn_{0.69}Sb_{0.035}$
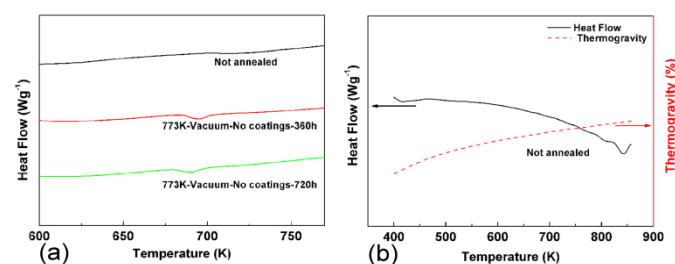
Fig. 3 (a) DSC results of samples annealed in vacuum taken over the temperature interval of 600–770 K, (b) DSC/TG results for the pristine, never annealed sample in the temperature range 400-850 K.

Journal Name

ARTICLE

Table 4 Actual compositions of BN-coated samples annealed in air (by EPMA).

Annealing conditions	773 K-Air-BN -360 h	773 K-Air-BN -720 h	823 K-Air-BN -360 h
Actual composition	$Mg_{2.10}Si_{0.27}Sn_{0.71}Sb_{0.017}$	$Mg_{2.11}Si_{0.26}Sn_{0.72}Sb_{0.015}$	$Mg_{1.83}Si_{0.32}Sn_{0.66}Sb_{0.019}$

The role of coatings

While operating $Mg_2Si_{1-x}Sn_x$ solid solutions under vacuum is not a good idea, their operation in air has its own challenges as the structure is prone to oxidation. To minimize Mg evaporation and prevent oxidation, we decided to protect $Mg_2Si_{1-x}Sn_x$ solid solutions by spraying them with BN, a common technique in the field of metal corrosion and protection.[42, 43]
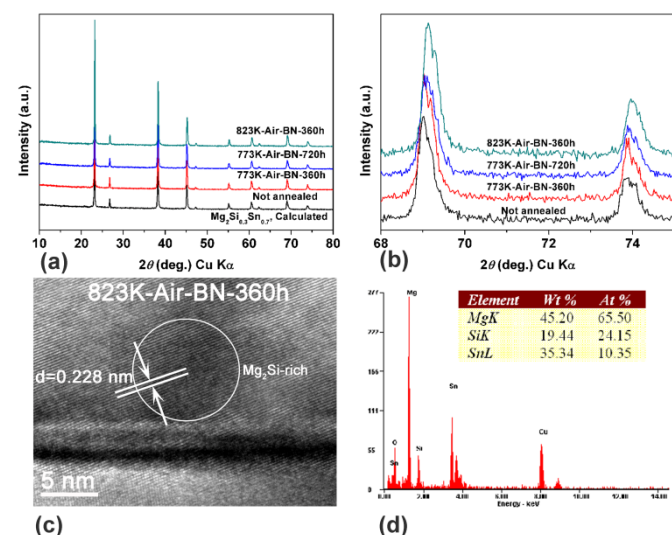

Fig. 4 (a) Powder XRD patterns of samples annealed in air with BN coating. (b) Enlarged XRD patterns within the angular range of 68-75°. (c)HRTEM image of the sample annealed at 823 K in air with BN coating. (d) EDX results for the selected region in fig. 4(c).

XRD patterns and EPMA results of BN-coated samples annealed at 773 K in air are shown in Fig. 4(a)-(b) and Table 4, respectively. Compared to the reference sample without annealing, the composition of the BN-coated sample annealed in air at 773 K has not changed. Heat flow plots and the microstructure (details presented in Figs. SI2(a) and SI3, respectively) showed no changes which indicates that the BN coating was highly effective in protecting $Mg_2Si_{1-x}Sn_x$ solid solutions from oxidation and the loss of Mg when operated in air. Furthermore, it is well known that both Mg_2Si and Mg_2Sn react with water[44, 45] and so do $Mg_2Si_{1-x}Sn_x$ solid solutions. Without coatings, lots of bubbles are observed after the sample was immersed in water for 1 min. After 24 h the surface of the sample was throughly corroded. While for the sample with BN coating, the surface of the sample (after removing the BN spray) is unchanged (see Fig.

SI4). So coating happen to be a practical solution in this case and provide an effective protection of $Mg_2Si_{1-x}Sn_x$ against steam corrosion.

The influence of annealing temperature on the composition and microstructure

As the $Mg_2Si_{1-x}Sn_x$ system is subject to a peritectic reaction at about 836 K,[46, 47] the composition and microstructure may show major changes after annealing around this temperature. Noting that the best TE performance is achieved around 750–800 K, the BN-coated samples were annealed in air at 823 K to check the thermal stability at this higher temperature.
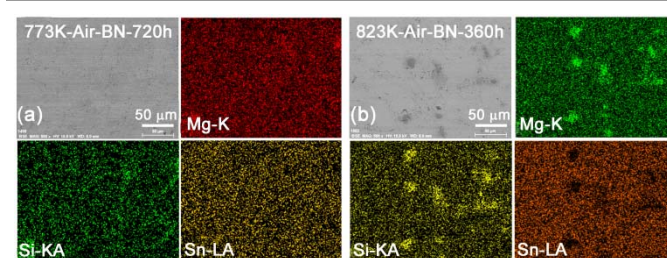
Fig. 5 Images and elemental distribution maps taken on polished surfaces of (a) a BN-coated sample annealed at 773 K in air, and (b) a BN-coated sample annealed at 823 K in air.

The XRD pattern of the BN-coated sample annealed at 823 K in air is shown in Fig. 4(a). The data show clearly that after annealing the structure is still single phase. However, this is not the case when the sample is characterized by back-scattered electron (BSE) images and EDX elemental distribution shown in Fig. 5. While a good chemical homogeneity prevails in the sample annealed at 773 K, Mg_2Si-rich phase is observed in the sample annealed at 823 K. To understand what happens, a small piece of sample not previously annealed was coated with the BN spray and subjected to the TGA/DSC analysis to check the thermal stability beyond 800 K. The results are shown in Fig. 3(b). An endothermic peak is apparent around 823–856 K in the DSC trace. As noted earlier, the phase diagram indicates a peritectic reaction taking place at ~ 836 K: $Mg_2Si_{0.3}Sn_{0.7} \rightarrow Mg_2Sn$-rich (L) + Mg_2Si-rich (S). Our DSC data suggest that the peritectic reaction actually begins at 823 K with the formation of Mg_2Sn-rich liquid phase and Mg_2Si-rich solid phase. However, the Mg_2Sn-rich liquid phase is not stable at high temperatures,[48-50] and decomposes into Mg and Sn with Mg evaporating quickly at this temperature and Sn peeling off

Please do not adjust margins

(details shown in Fig. SI2(b)) due to the thermal stress and the mismatch between thermal expansion coefficients of Sn and the matrix. Numerous pores with the size of 10-20 μm left in the sample (shown in Fig. 6), which is the evidence of this decomposition process. This is also verified by the EPMA (shown in Table 4). In addition, HRTEM results indicates nanoprecipatate is observed after annealing at 823 K, which is rich in Mg_2Si as shown in Fig. 4(c)-(d). Changes in the composition and microstructure will play an important role regarding TE properties of $Mg_2Si_{1-x}Sn_x$ solid solutions, as discussed in the following section.
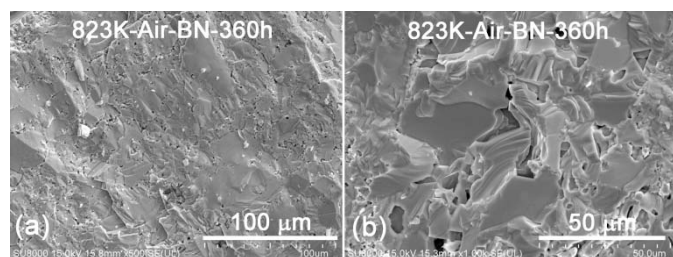

Fig. 6 Microstructure of the BN-coated sample annealed in air at 823 K.
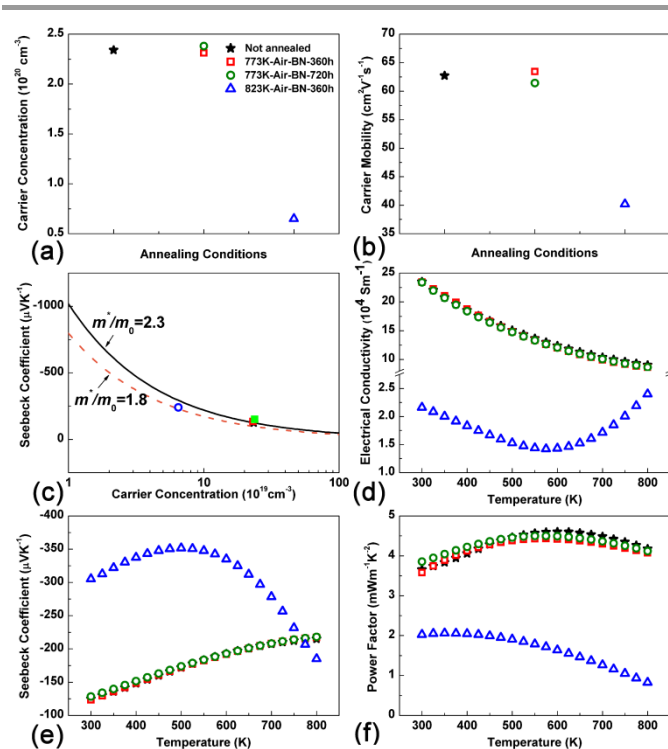
Transport properties

Fig. 7 (a) Carrier concentration, (b) carrier mobility,and (c) the Pisarenko plot (S vs. n) at 300 K, (d) electrical conductivity, (e) Seebeck coefficient and (f) power factor as a function of temperature.

The key transport parameters such as the carrier concentration, the carrier mobility, and the Pisarenko plot (S vs. n) at 300 K, the electrical conductivity, the Seebeck coefficient and the power factor as a function of temperature are shown in Fig. 7. While annealing of BN-coated samples at 773 K has essentially no effect on transport properties (measured relative to the sample not annealed at all), annealing at 823 K decreases the carrier concentration dramatically due to the loss of Mg and Sn in the matrix. As the carrier concentration of $Mg_2Si_{1-x}Sn_x$ is very sen-

sitive to the composition especially the Mg content, the deficiency of Mg would induce lots of Mg vacancies, counteracting the doping effect of Sb, thus the carrier concentration of the sample annealed at 823 K is much lower than that of unannealed sample.[24, 35, 51]. Moreover, the carrier mobility is also degraded significantly as a result of structural changes and the emergence of the Mg_2Si-rich nanostructure which strongly scatters electrons.[52-54] The simultaneous decrease in the carrier concentration and the carrier mobility results in an inferior electrical conductivity of the sample annealed at 823 K. The Pisarenko plot in Fig. 7(c) suggest a decrease in the effective mass of the sample annealed at 823 K, which is also due to the composition change as mentioned above. And this is consistent with the result of W. Liu et al[27] and X. J. Tan et al,[28] which shows that the deviation in composition from $x = 0.65$-0.70, especially with high Mg_2Si ratio, would lower the effective mass. Hand in hand with the reduced carrier concentration, the Seebeck coefficient increases by about 60%. However, this enhancement in the Seebeck coefficient does not compensate for the degraded electrical conductivity and the power factor of the sample annealed at 823 K decreased significantly.
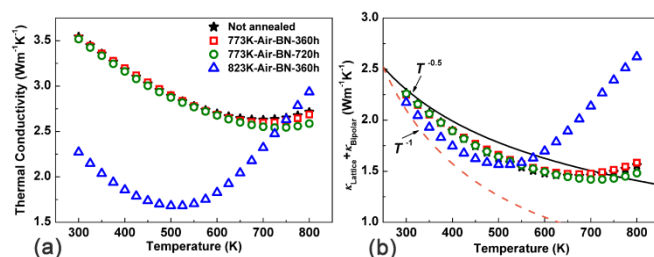

Fig. 8 (a) Thermal conductivity, (b) sum of the lattice thermal conductivity and the bipolar part as a function of temperature.

The total thermal conductivity and the lattice thermal conductivity ($\kappa_{Lattice}$) combined with the bipolar part ($\kappa_{Bipolar}$) are shown in Figs. 8(a)-(b). The latter was calculated by subtracting the electronic thermal conductivity $L\sigma T$ from the total thermal conductivity. The Lorenz number L (shown in Fig. SI5(a))was calculated based on the single parabolic band (SPB) model under the relaxation time approximation.[29] The values of sample annealed at 773 K are consistent with the results reported by H. L. Gao et al,[55] while the value of sample annealed at 823 K is much lower owing to the lower carrier concentration. The lattice thermal conductivity of the BN-coated samples annealed at 773 K in air very closely matches the $T^{-0.5}$ temperature dependence of the sample never subjected to annealing. This again confirms that annealing a protected sample of $Mg_2Si_{1-x}Sn_x$ to temperatures of 773 K does not alter its transport properties and alloy scattering continues to be the dominant scattering mode of heat conducting phonons.[56] The lower lattice thermal conductivity of the sample annealed at 823 K in the temperature range below 550 K is due to the presence of nano-scale (~ 20 nm) inclusions of the Mg_2Si-rich phase, see Fig. 4(c), which apparently enhances phonon scattering. Above 550 K, the ambipolar term takes over and the thermal conductivity rapidly increases in accord with the turnover observed in the Seebeck coefficient in Fig. 7(e).
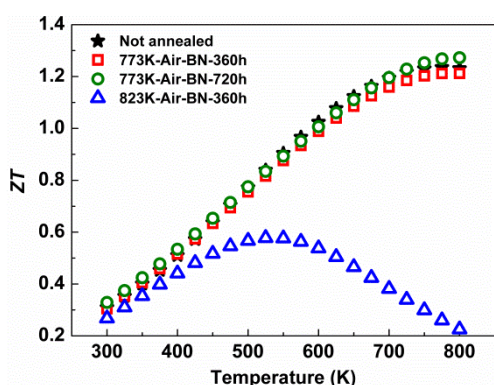
ARTICLE   **Journal Name**

Fig. 9 *ZT* values of samples annealed under different conditions as a function of temperature.

The *ZT* value as a function of temperature is shown in Fig. 9. Since the composition and microstructure of BN-coated samples annealed at 773 K in air remain unchanged, so do the key transport parameters and the *ZT* value of such samples is essentially identical to that of the pristine material never subjected to any annealing treatment. In contrast, the *ZT* value of the sample with an identical chemical composition but annealed at 823 K has sharply decreased and its peak value shifted from 750 K down to about 550 K. These results indicate that $Mg_2Si_{1-x}Sn_x$ solid solutions should work well as long as the thermoelectric elements are properly protected and the operational range does not extend beyond 800 K.

Conclusions

Thermal stability of *n*-type $Mg_{2.16}(Si_{0.3}Sn_{0.7})_{0.98}Sb_{0.02}$ solid solutions was studied as a function of heat treatment conditions. Specifically, we explored the influence of an annealing temperature, annealing time, annealing atmosphere, and preventive coatings. The key factors which dominate the thermal stability of $Mg_2Si_{1-x}Sn_x$ solid solutions are the annealing atmosphere, preventive coatings, and temperature. The rate at which Mg evaporates and the ultimate composition of $Mg_2Si_{1-x}Sn_x$ solid solutions depend critically on the annealing temperature and the environment at which annealing takes place. Applying coatings that protect thermoelectric legs, such as BN sprays, is an effective way to minimize oxidation and steam corrosion and should assure successful operation to temperatures of about 800 K.

Acknowledgements

Notes and references

1 F. J. DiSalvo, Science, 1999, 285, 703-706.
2 L. E. Bell, Science, 2008, 321, 1457-1461.
3 D. K. C. MacDonald, Thermoelectricity: an introduction to the principles, Courier Corporation, 2006.
4 H. J. Goldsmid, Introduction to thermoelectricity, Springer Science & Business Media, 2009.
5 G. J. Snyder and E. S. Toberer, Nature materials, 2008, 7, 105-114.
6 J. R. Sootsman, D. Y. Chung and M. G. Kanatzidis, Angewandte Chemie International Edition, 2009, 48, 8616-8639.
7 Y. Zhang and G. D. Stucky, Chemistry of Materials, 2014, 26, 837-848.
8 J. de Boor, C. Gloanec, H. Kolb, R. Sottong, P. Ziolkowski and E. Müller, Journal of Alloys and Compounds, 2015, 632, 348-353.
9 W. Liu, Q. Jie, H. S. Kim and Z. Ren, Acta Materialia, 2015, 87, 357-376.
10 W. He, G. Zhang, X. Zhang, J. Ji, G. Li and X. Zhao, Applied Energy, 2015, 143, 1-25.
11 W. Wunderlich, Energy Harvesting and Systems, 2015, 2, 37-46.
12 H. Gao, T. Zhu, X. Liu, L. Chen and X. Zhao, Journal of Materials Chemistry, 2011, 21, 5933-5937.
13 E. Nikitin, Zh. Tekh. Fiz, 1958, 28, 23-25.
14 E. Nikitin, V. Bazanov and V. Tarasov, Soviet Physics Solid State, 1962, 3, 2648-2651.
15 V. Zaitsev, E. Tkalenko and E. Nikitin, Soviet Physics Solid State, 1969, 11, 221-224.
16 W. Liu, Q. Zhang, X. Tang, H. Li and J. Sharp, Journal of Elec Materi, 2011, 40, 1062-1066.
17 W. Liu, Q. Zhang, K. Yin, H. Chi, X. Zhou, X. Tang and C. Uher, Journal of Solid State Chemistry, 2013, 203, 333-339.
18 P. Zwolenski, J. Tobola and S. Kaprzyk, Journal of Elec Materi, 2011, 40, 889-897.
19 J. J. Pulikkotil, D. J. Singh, S. Auluck, M. Saravanan, D. K. Misra, A. Dhar and R. C. Budhani, Physical Review B, 2012, 86, 155204.
20 N. Farahi, M. VanZant, J. Zhao, S. T. John, S. Prabhudev, G. A. Botton, J. R. Salvador, F. Borondics, Z. Liu and H. Kleinke, Dalton Transactions, 2014, 43, 14983-14991.
21 V. Zaitsev, M. Fedorov, E. Gurieva, I. Eremin, P. Konstantinov, A. Samunin and M. Vedernikov, Physical Review B, 2006, 74.
22 V. Zaitsev and M. Fedorov, Semiconductors, 1995, 29, 490-497.
23 X. Liu, T. Zhu, H. Wang, L. Hu, H. Xie, G. Jiang, G. J. Snyder and X. Zhao, Advanced Energy Materials, 2013, 3, 1238-1244.
24 G. Jiang, J. He, T. Zhu, C. Fu, X. Liu, L. Hu and X. Zhao, Advanced Functional Materials, 2014, 24, 3776-3781.
25 W. Liu, X. Tang, H. Li, K. Yin, J. Sharp, X. Zhou and C. Uher, Journal of Materials Chemistry, 2012, 22, 13653-13661.
26 Q. Zhang, J. He, T. Zhu, S. Zhang, X. Zhao and T. Tritt, Applied Physics Letters, 2008, 93, 102109.
27 W. Liu, X. Tan, K. Yin, H. Liu, X. Tang, J. Shi, Q. Zhang and C. Uher, Physical Review Letters, 2012, 108.
28 X. J. Tan, W. Liu, H. J. Liu, J. Shi, X. F. Tang and C. Uher, Physical Review B, 2012, 85.
29 W. Liu, H. Chi, H. Sun, Q. Zhang, K. Yin, X. Tang, Q. Zhang and C. Uher, Physical Chemistry Chemical Physics, 2014, 16, 6893-6897.
30 D. R. Brown, T. Day, T. Caillat and G. J. Snyder, Journal of Elec Materi, 2013, 42, 2014-2019.

31 H. Yin, B. L. Pedersen and B. B. Iversen, European Journal of Inorganic Chemistry, 2011, 2011, 2733-2737.

32 L. Zhang and J. Sakamoto, Materials Chemistry and Physics, 2013, 138, 601-607.

33 J. Bourgeois, J. Tobola, B. Wiendlocha, L. Chaput, P. Zwolenski, D. Berthebaud, F. Gascoin, Q. Recour and H. Scherrer, Functional Materials Letters, 2013, 06, 1340005.

34 G. Skomedal, N. R. Kristiansen, M. Engvoll and H. Middleton, Journal of Elec Materi, 2013, 1-6.

35 W. Liu, X. Tang, H. Li, J. Sharp, X. Zhou and C. Uher, Chemistry of Materials, 2011, 23, 5256-5263.

36 Q. Zhang, L. Cheng, W. Liu, Y. Zheng, X. Su, H. Chi, H. Liu, Y. Yan, X. Tang and C. Uher, Physical Chemistry Chemical Physics, 2014, 16, 23576-23583.

37 Z. Du, T. Zhu, Y. Chen, J. He, H. Gao, G. Jiang, T. M. Tritt and X. Zhao, Journal of Materials Chemistry, 2012, 22, 6838.

38 G. H. Grosch and K.-J. Range, Journal of alloys and compounds, 1996, 235, 250-255.

39 S.-W. Chen, C.-C. Chen, W. Gierlotka, A.-R. Zi, P.-Y. Chen and H.-J. Wu, Journal of Elec Materi, 2008, 37, 992-1002.

40 H. Okamoto, Journal of Phase Equilibria and Diffusion, 2012, 33, 347-347.

41 Y. Gelbstein, J. Tunbridge, R. Dixon, M. J. Reece, H. Ning, R. Gilchrist, R. Summers, I. Agote, M. A. Lagos and K. Simpson, Journal of Elec Materi, 2014, 43, 1703-1711.

42 A. E. Hughes, I. S. Cole, T. H. Muster and R. J. Varley, NPG Asia Materials, 2010, 2, 143-151.

43 B. Bonnetot, F. Guilhon, J. Viala and H. Mongeot, Chemistry of materials, 1995, 7, 299-303.

44 W. Robertson and H. Uhlig, Journal of The Electrochemical Society, 1949, 96, 27-42.

45 Alfa Aesar, Material Safety Data Sheet, Magnesium Silicide (Alfa Aesar, 4 November 2010)).

46 I.-H. Jung, D.-H. Kang, W.-J. Park, N. J. Kim and S. Ahn, Calphad, 2007, 31, 192-200.

47 A. Kozlov, J. Gröbner and R. Schmid-Fetzer, Journal of Alloys and Compounds, 2011, 509, 3326-3337.

48 H. Caulfield and D. Hudson, Solid State Communications, 1966, 4, 299-301.

49 G. Raynor, Metal Science, 1975, 9, 430-431.

50 D. Zhou, J. Liu, S. Xu and P. Peng, Computational Materials Science, 2012, 51, 409-414.

51 G. Nolas, D. Wang and M. Beekman, Physical Review B, 2007, 76.

52 D. Pshenai-Severin, M. Fedorov and A. Y. Samunin, Journal of Elec Materi, 2013, 42, 1707-1710.

53 P. N. Alboni, X. Ji, J. He, N. Gothard and T. M. Tritt, Journal of Applied Physics, 2008, 103, 113707.

54 W. Xie, S. Wang, S. Zhu, J. He, X. Tang, Q. Zhang and T. M. Tritt, Journal of Materials Science, 2013, 48, 2745-2760.

55 H. Gao, T. Zhu, X. Zhao and Y. Deng, Dalton Trans, 2014, 43, 14072-14078.

56 P. Klemens, Physical Review, 1960, 119, 507.